 DOI: 10.1002/maco.201508709

Influence of annealing temperature on sensitisation behaviour and corrosion properties of an Al-6.8 wt% Mg alloy

T. Radetić*, M. Popović, B. Jegdić and E. Romhanji

Influence of annealing temperature on β-(Al_3Mg_2) phase precipitation and corrosion properties of sensitised Al-6.8 wt% Mg alloy is investigated. Sensitisation of specimens annealed at 320 °C results in IGC and SCC susceptibility. Microstructural characterization shows fine precipitation of Mg-rich phase forming nearly continuous film at grain boundaries, despite small precipitated fraction (0.5%), and grain boundary faceting. Sensitised specimens annealed at 265 °C are IGC susceptible, but SCC resistant. Precipitation at grain boundaries is discrete, although the precipitated fraction is greater (3%) than in specimens annealed at 320 °C. Potentiodynamic measurements show that of all measured parameters, charge density is in the strongest correlation with the NAMLT and SSRT results.

1 Introduction

Non-heat treatable Al–Mg alloys (5xxx series) have a wide range of applications as they are used in production of marine, auto and aircraft parts, storage tanks, cryogenics, drilling rigs, transportation equipment as well as in packaging industry due to the favourable combination of strength, formability, weldability and corrosion resistance in atmospheric conditions [1,2]. An increase in Mg content improves mechanical properties of the Al–Mg alloys [3], but it also contributes to increased intergranular corrosion (IGC) and stress corrosion cracking (SCC) susceptibility if the alloy is exposed to temperatures in a 60–200 °C range [4]. All the more, a long-term natural ageing can give rise to an IGC susceptible material if magnesium content in the alloy is sufficiently high [5]. It is accepted that the IGC and SCC susceptibility increase is due to precipitation of anodic β-(Al_3Mg_2) phase at grain boundaries in the process known as sensitisation, although there are reports of SCC occurrence even in the absence of β-(Al_3Mg_2) phase precipitation [6,7]. Sensitisation effects are uncommon in the alloys with Mg content below 3.5 wt%, but as the Mg content rises from 3.4 to 4 wt%, there is an abrupt increase in the IGC susceptibility [8]. Further increase in the Mg content leads to linear, but less steep susceptibility increase [8]. During sensitisation of recrystallised Al–Mg alloys, the precipitation kinetics and morphology of β-(Al_3Mg_2) phase are affected by Mg content. In the alloys containing over 7 wt% Mg, a continuous film forms at the grain boundaries [9,10] while discrete particles characterise the alloys with 4–5 wt% Mg that underwent same or similar processing [9,11,12]. Besides Mg content, key factors controlling the precipitation of the β-(Al_3Mg_2) phase in the Al–Mg alloys are considered to be sensitisation temperature and time; their increase increases fraction and continuity of the grain boundary β-(Al_3Mg_2) phase [11,13–16]. However, a thermo-mechanical treatment has an influence on β-(Al_3Mg_2) phase precipitation and can alter corrosion response of Al–Mg alloys [17–23]. Precipitation of the β-(Al_3Mg_2) phase appears to be more advanced in deformed [14] than in recrystallised microstructure [11] of AA 5083 alloy-type materials that underwent similar sensitisation treatment. Grain boundary crystallography has an influence on nucleation and growth as well as morphology of β-(Al_3Mg_2) phase [5,19,24,25].

Most of the published body of research has been directed on studies of thermo-mechanical treatment and sensitisation behaviour of commercial Al–Mg alloys with Mg content below 6 wt%. Previous work on non-commercial Al-6.8 wt% Mg alloy [26–28] showed that, in addition to good mechanical properties and formability, and despite high Mg content, suitable thermo-mechanical treatment could result in a favourable corrosion response of the alloy.

In this study, the effect of final annealing temperature on the microstructure development and precipitation of β-(Al_3Mg_2) phase during sensitisation of the Al-6.8 wt% Mg alloy has been investigated. The susceptibility towards SCC and IGC as well as electrochemical properties of the alloy after different thermal

T. Radetić, M. Popović, E. Romhanji
Department of Metallurgical Engineering, Faculty of Technology and Metallurgy, University of Belgrade, Karnegijeva 4, POB 35-03, 11 120, Belgrade (Serbia)
E-mail: tradetic@tmf.bg.ac.rs

B. Jegdić
ICTM-Department of Electrochemistry, University of Belgrade, Njegoševa 12, 11 120, Belgrade (Serbia)

treatments have been assessed and correlated with the morphology of precipitated β-(Al_3Mg_2) phase.

2 Materials and methods

2.1 Material

The non-commercial Al-6.8 wt% Mg alloy was supplied in a fully annealed condition (O-temper with a yield strength of 161 MPa, ultimate tensile strength of 343 MPa and elongation of 26%) by Impol-Seval Aluminium Rolling Mill – Serbia. Chemical composition of the alloy is given in Table 1.

The as-received alloy underwent further thermo-mechanical treatment in the laboratory that included cold rolling, annealing in a temperature range of 225–320 °C and sensitisation for 7 days at 100 °C. The alloy processing sequence is shown in Fig. 1.

2.2 SCC and IGC susceptibility tests

The SCC susceptibility of sensitised specimens was evaluated by slow strain rate testing (SSRT). Specimens were cut in long-transverse orientation and had dimensions: gauge length of 25 mm and width of 6.25 mm. The SSRT was performed in dry air (at an initial strain rate of 6.7×10^{-4}/s) and in 2 wt% NaCl + 0.5 wt% Na_2CrO_4 aqueous solution (at an initial strain rate of 3.3×10^{-5}/s). Relative elongation in the corrosive environment (El_{SCC}) was compared with the corresponding in the dry air (El_{air}), and the SCC susceptibility was determined by the elongation loss (El_{loss}). El_{loss} was calculated according to the formula: $El_{loss} = [1 - (El_{scc}/El_{air})] \times 100\%$.

Table 1. Chemical composition of the studied Al-6.8 wt% Mg alloy, wt%

Mg	Mn	Fe	Si	Cr	Zn	Cu	Ti	Al
6.80	0.51	0.20	0.10	0.001	0.003	0.001	0.054	Bal.

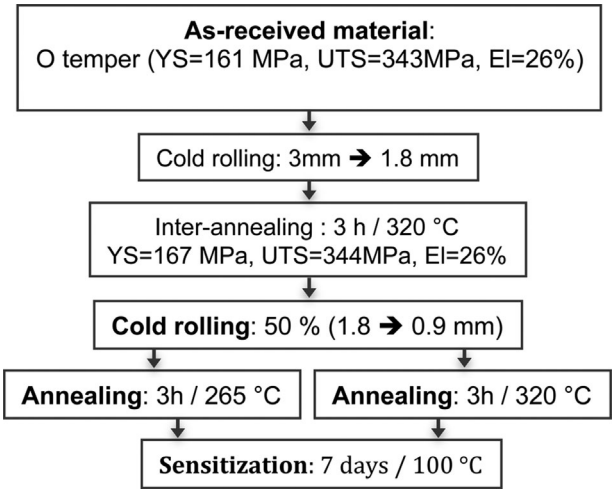

Figure 1. Processing chart of the studied Al-6.8 wt% Mg alloy

IGC susceptibility of selected states was determined by nitric acid mass loss test (NAMLT) according to the ASTM G67 standard.

All tests were performed at least three times for each state.

2.3 Microstructural characterisation

Microstructural characterisation of the selected states included light optical microscopy (LOM), scanning electron microscopy (SEM) and transmission electron microscopy (TEM) and microanalysis. Specimens for LOM were etched in a solution of orthophosphoric acid (10 mL H_3PO_4 (85 wt%) + 90 mL H_2O) at 50 °C for 20 s to reveal β-(Al_3Mg_2) phase precipitation at the grain boundaries. SEM characterisation was conducted in JEOL JSM-6610LV at 20 kV and FEG Tescan at 20 kV. SEM specimens were mechanically polished, and those characterised at higher magnifications were etched in ammonium persulfate, $(NH_4)_2S_2O_8$ dissolved in de-ionised water to reveal β-(Al_3Mg_2) phase [29]. Specimens for a TEM characterisation were mechanically thinned to 100 μm and then electropolished in a CH_3OH:HNO_3 = 3:1 solution in Fischione Twin Jet Polisher. The electropolishing conditions were U = 10 V, I = 21 mA and T = −35 °C. TEM characterisation and microanalysis were conducted in a JEOL 100CX at 100 kV and Philips CM200 microscopes at 200 kV. The Philips CM200/FEG microscope was equipped with energy dispersive spectroscopy (EDS) detector and in-situ heating unit.

Since sensitisation temperature of 100 °C is characterised by a very slow kinetics of β-(Al_3Mg_2) phase precipitation, it is not adequate for in situ heating experiments. Hence, 200 °C was selected for in situ heating, due to faster precipitation kinetics while maintaining sufficient supersaturation of the Al solid solution. Additionally, Al radiation damage becomes insignificant at 200 °C. However, thin foil effect – contribution of surface diffusion to precipitation processes – was unavoidable.

2.4 Electrical resistivity measurements

The electrical resistivity measurements were conducted to assess the extent of the precipitation of β-(Al_3Mg_2) phase during the sensitisation according to the method described in Refs. [27,30]. The measurements were performed with a commercial eddy current Foerster Sigmatest 2.069 instrument, at operating frequency of f = 480 kHz. The absolute accuracy of the instrument was within ±0.5% of measured value. At least 10 measurements were performed on each tested specimen.

2.5 Electrochemical tests

Pitting potentiodynamic polarisation tests were performed on selected states using Galvanostat/Potentiostat Bio-Logic SP 200 instrument. Standard three-electrode cell arrangement was used: tested aluminium alloy was the working electrode while the counter electrode was a platinum mesh whose surface area was considerably greater than that of the working electrode. The reference electrode was a saturated calomel electrode (SCE). The test was carried out in 3 wt% NaCl aqueous solution under ambient conditions. The potentiodynamic polarisation for all

measurements started from the cathodic potential −0.15 V *versus* open circuit potential (E_{ocp}) and reversed when a current density of 500 μA/cm^2 was reached. The scanning was terminated at the initial open circuit potential. Sweep rate of 1.0 mV/s was applied after establishing the constant E_{ocp} (up to 30 min). Pitting potential (E_{pitt}), protection potential (E_{prot}), i.e., potential at which growth of formed pits stops, and charge density (q), defined as a charge passed between E_{pitt} and E_{prot}, were determined by analysis of the polarisation curves.

The linear polarisation resistance (LPR) test was performed in the same cell, in 3 wt.% NaCl aqueous solution under ambient conditions. Potential scan between −15 mV and +15 mV (from cathodic to anodic) over E_{ocp} was performed at 0.167 mV/s sweep rate. The open circuit potential of working electrodes was monitored up to 30 min prior application of LPR technique. All electrochemical measurements were performed at least three times for each state.

3 Results

3.1 IGC and SCC susceptibility

The elongation loss (El_{loss}), in the SSRT, of the specimens annealed at 225–320 °C and sensitised for 7 days at 100 °C, is shown in Fig. 2. Specimens annealed at lower temperatures, 225–285 °C, essentially have no elongation loss while the El_{loss} of the specimens annealed at 320 °C is over 80%, rendering them SCC susceptible. Further characterization was conducted on the specimens annealed at 265 and 320 °C, since those annealing temperatures give rise to an SCC resistant and susceptible material after the sensitisation, respectively.

Results of the NAML test for the selected states are summarised in Table 2. Mass loss of only annealed specimens is within a limit of IGC resistant states, but the specimens annealed at 265 °C have a greater loss than ones annealed at 320 °C. Sensitisation reversed the trend. The mass loss of 65.7 ± 1.9 mg/cm^2 positions sensitised specimens annealed at 320 °C deep inside the field of IGC susceptible states. On the contrary, sensitised specimens annealed at 265 °C with the mass loss of 26.4 ± 0.9 mg/cm^2 are on the borderline. Correlation between the mass loss in NAML test (Table 2) and SCC susceptibility (Fig. 2) is concurrent with the other reports [17,18,24] indicating that the IGC susceptible specimens with the mass loss below 40 mg/cm^2 might not be prone towards SCC.

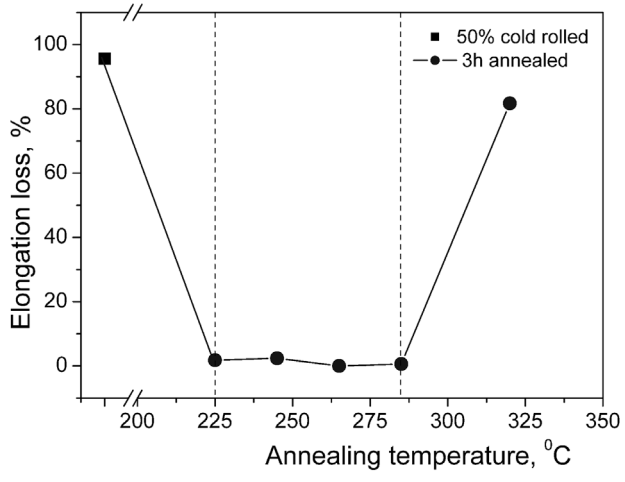

Figure 2. Elongation loss (El_{loss}) as a function of the annealing temperature of the specimens sensitised for 7 days at 100 °C

Table 2. Mass loss after the NAMLT as a function of the thermal treatment

Specimen	Mass loss[a] (mg/cm^2)
3 h/320 °C	7.3 ± 0.1
3 h/265 °C	13.8 ± 2.2
3 h/320 °C + 7 days/100 °C	65.7 ± 1.9
3 h/265 °C + 7 days/100 °C	26.4 ± 0.9

[a]According to ASTM 67 Standard, mass loss <15 mg/cm^2 corresponds to IGC resistant states, while mass loss >25 mg/cm^2 corresponds to IGC susceptible states. In the intermediate region, microscopic characterisation is necessary to determine IGC susceptibility.

3.2 Microstructure

3.2.1 Annealing at 320 °C

Microstructure of the alloy annealed at 320 °C is fully recrystallised with smooth, curved grain boundaries (Fig. 3). No β-(Al_3Mg_2) phase has been detected (Fig. 4a), but a few tiny particles in the grain boundaries (Fig. 3b). It is likely that those particles precipitated while cooling in the air. That state is associated with the greatest electrical resistivity (Table 3) implying a high concentration of Mg in the solid solution [27,28].

During the sensitisation treatment, Mg-rich phase precipitates at the grain boundaries (Fig. 4b) in the form of a film less than 40 nm thick (Fig. 5). Crystal structure of the precipitated phase remains elusive, due to the faint diffraction spots that prevented unambiguous phase identification. Although it is generally considered that the product of sensitisation is β-(Al_3Mg_2) phase, recent study [31] suggests that the Mg-rich phase precipitated during sensitisation at low temperatures is actually β′-(Al_3Mg_2).

The area fraction of the precipitated phase is assessed to be 0.5%, based on the measurement the total length of grain boundaries etched by orthophosphoric acid and using thickness of the film (10–40 nm) determined by TEM characterisation. That value is close to the fraction determined from the electrical resistivity measurements of 0.35% [27].

TEM characterization of grain boundaries after the sensitisation reveals that the film exhibited non-uniform contrast (Fig. 6a) and is not continuous but consists of very fine crystallites (Fig. 6b). Moreover, the precipitation adopted 'saw-tooth' morphology clearly seen at higher magnification (Fig. 6c). The grain boundary precipitation introduces strain fields in the surrounding matrix (Fig. 6d) with a period close to the length of the 'tooth'. However, there is no strain on the segment of the grain boundary devoid of precipitation (pointed by the arrows in Fig. 6a, c–e). Under different imaging conditions, distorted grain boundary fringes and offsets, indicating facets and steps are observed in the grain boundary segment covered with the

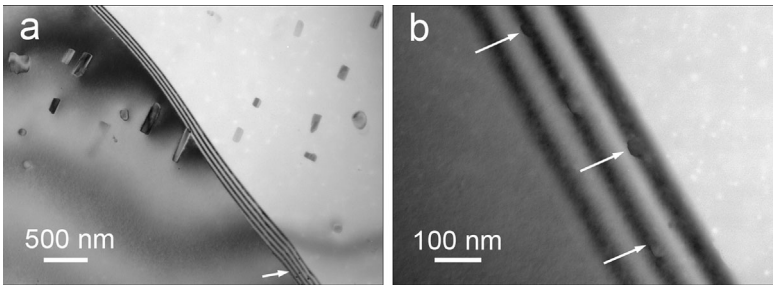

Figure 3. Bright field TEM images of: (a) grain boundary in the specimen annealed 3 h at 320 °C; (b) the section of the grain boundary pointed by arrow in (a), showing a few very fine particles

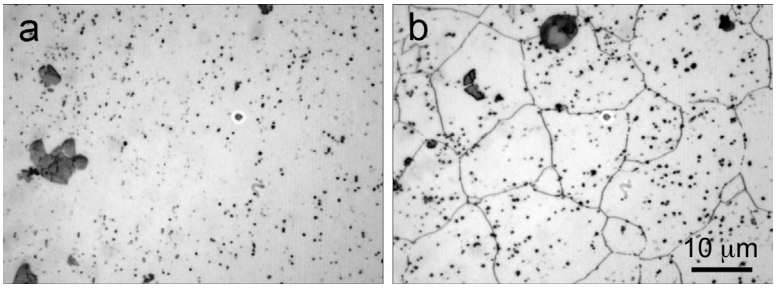

Figure 4. Optical micrographs of the specimens etched by orthophosphoric acid to reveal β-(Al_3Mg_2) phase at grain boundaries. Specimens annealed for 3 h at 320 °C, before (a) and after (b) sensitisation

precipitates (Fig. 6e) while the segment free of the precipitation has undisturbed grain boundary fringes.

Faceting of the grain boundaries appears to be a general feature of the specimens annealed at 320 °C after the sensitisation (Fig. 6f). In situ heating experiment (Fig. 7) provided insight into the grain boundary transformation. Initially, the grain boundary had straight, undisturbed fringe contrast and no grain boundary precipitation (Fig. 7a). Fine crystallites precipitated after 7 min at 200 °C (Fig. 7b) and continued to grow along the boundary (Fig. 7c). The precipitation introduces distortion and offsets into the boundary fringes indicating incipient steps (Fig. 7d).

Deformation of 2% prior sensitisation affects the morphology of precipitated β-(Al_3Mg_2) phase (Fig. 8). Larger gaps in the grain boundary coverage and break up of a continuous film, as well as thicker lenticular grain boundary precipitates, are observed.

3.2.2 Annealing at 265 °C

Lower electrical resistivity of the specimens annealed at 265 °C than ones annealed at 320 °C (Table 3) indicates precipitation of Mg out of the solid solution. The precipitation of the β-(Al_3Mg_2) phase takes place at the grain boundaries as well as in grain interiors in a form of coarse but discrete particles (Fig. 9a). TEM observations of high dislocation density and presence of cell and subgrain structure (Fig. 10a) are in agreement with reported variation of mechanical properties indicating incomplete recrystallisation in that state [26].

Table 3. Electrical resistivity as a function of the annealing conditions

Specimen	Electrical resistivity (μΩ cm)
3 h/320 °C	6.71 ± 0.009
3 h/265 °C	6.53 ± 0.007
3 h/320 °C + 7 days/100 °C	6.69 ± 0.008
3 h/265 °C + 7 days/100 °C	6.44 ± 0.012

Sensitisation results in an increase in density and size of the precipitated β-(Al_3Mg_2) phase (Fig. 9b), but the particles remain discrete to a large extent. Due to the large particle size, precipitates' area fraction has been determined by direct measurements on the SEM micrographs with a sufficient sampling and statistics. The result, 3% area fraction, is in a good agreement with the electrical resistivity measurements that gave 2.65% [27,28].

Grain boundary precipitates have an irregular shape and are extended along the grain boundary and into one of the grains (Fig. 10b). Sponge-like morphology, reported by Refs. [29,32], characterises the grain boundary precipitation. The TEM specimens preparation method introduced some amorphisation and dissolution of anodic β-(Al_3Mg_2) phase [33], but a number of the particles remained crystalline. The analysis of diffraction patterns reveals Fd3m crystal structure of β-(Al_3Mg_2) phase (Fig. 10c). The same crystal structure has been ascribed to the massive, heavily twinned precipitates nucleated at pre-existing intermetallic particles in the grain interiors.

3.3 Electrochemistry

Characteristic electrochemical parameters are given in Table 4 and potentiodynamic polarisation curves of the selected states

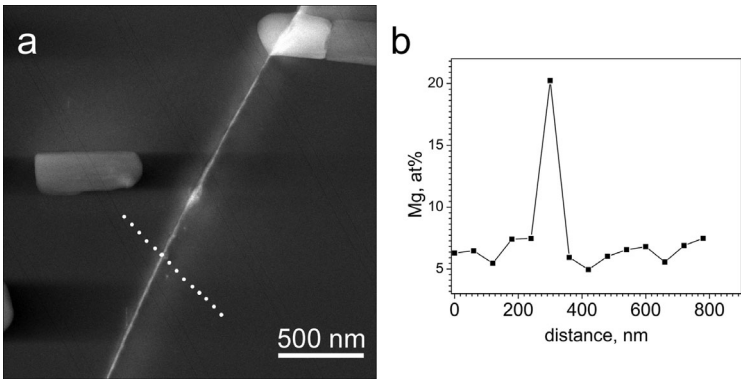

Figure 5. STEM image of the grain boundary (a) and corresponding EDS profile (b) showing Mg enrichment at the grain boundary. Specimen was annealed for 3 h at 320 °C and sensitised

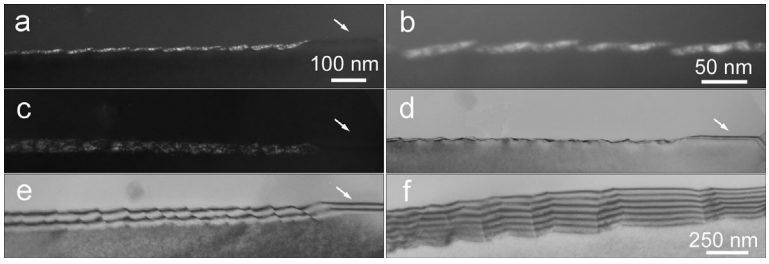

Figure 6. TEM micrographs of a grain boundary precipitation after the sensitisation of the specimen annealed 3 h/320 °C. (a–e) Micrographs of the same grain boundary under different imaging conditions: (a) and (b) dark field images, the boundary is 'edge-on'; (c) dark field, the boundary is inclined to the electron beam; (d) bright field, the grain boundary is 'edge-on'; (e) bright field micrograph of the inclined boundary. (f) Bright field image of another grain boundary with well-defined facets

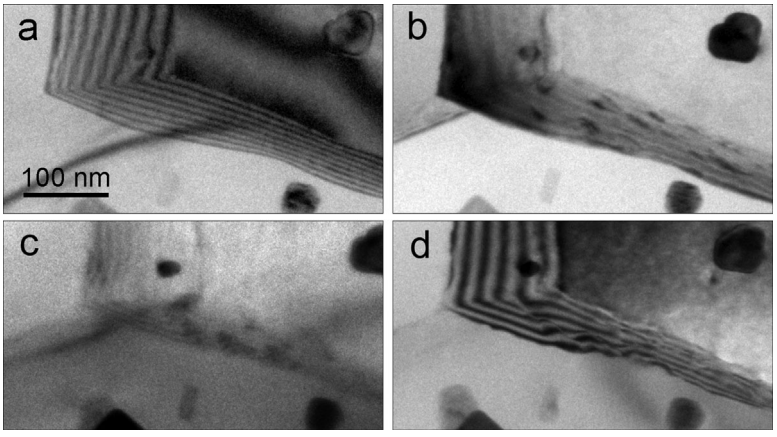

Figure 7. BF TEM images of a grain boundary triple junction during in-situ heating: (a) room temperature; (b) 7 min at 200 °C; (c) 45 min at 200 °C; (d) 45 min at 200 °C, visible grain boundary fringes

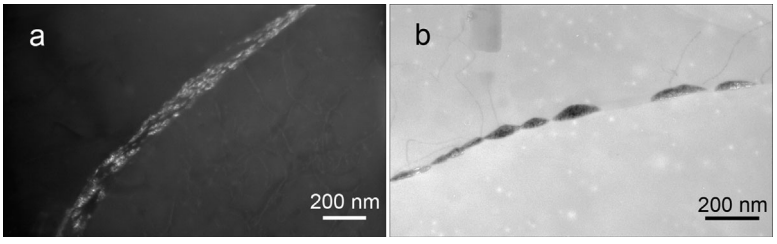

Figure 8. TEM micrographs of grain boundary precipitation in the specimen annealed 3 h at 320 °C and deformed 2% prior to the sensitisation: (a) dark field image; (b) bright field image

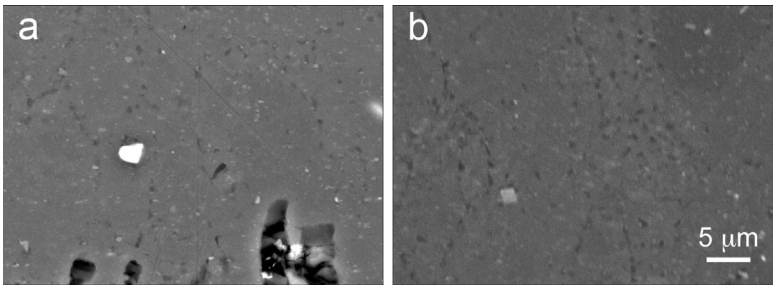

Figure 9. Backscattered electron SEM images of the specimens annealed 3 h at 265 °C prior (a) and after the sensitisation (b), showing precipitation of β-(Al_3Mg_2) phase

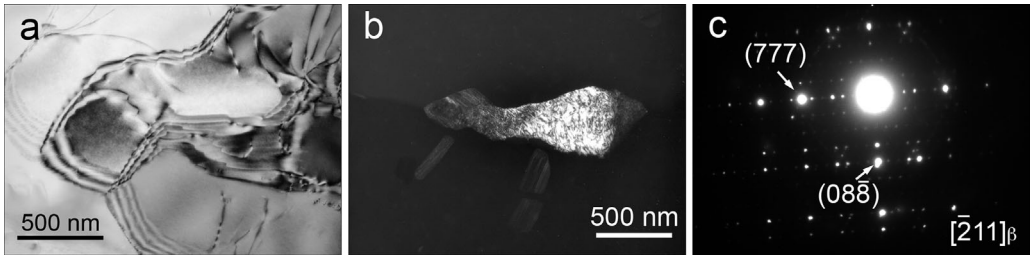

Figure 10. (a) Bright field TEM image of subgrain microstructure in the specimen annealed 3 h/265 °C. (b) Dark field TEM image of grain boundary β-(Al_3Mg_2) phase particle and corresponding diffraction pattern (c). The specimen was annealed 3 h/265 °C and sensitised

Table 4. Values of electrochemical parameters determined by electrochemical measurements as a function of the thermal treatment

Specimen	E_{ocp} *versus* SCE (mV)	E_{pitt} *versus* SCE (mV)	E_{prot} *versus* SCE (mV)	$E_{pitt} - E_{prot}$ (mV)	q (mC/cm^2)	b_a (mV/dec)	b_c (mV/dec)	R_p (kΩ cm^2)	j_{corr} (μA/cm^2)
3 h/320 °C	−827	−782	−800	18	13.2	34	550	53	0.26
3 h/265 °C	−818	−792	−810	18	11.4	32	450	47	0.28
3 h/320 °C + sensits	−820	−768	−798	30	23.5	36	550	33	0.45
3 h/265 °C + sensits	−834	−792	−807	15	10.6	32	450	43	0.30

are shown in Figure 11. The anodic polarisation curves do not show a sharp increase in the current density that would indicate the position of the pitting potential (E_{pitt}), similarly to the behaviour observed in some Al–Mg and other Al alloys [8,34–36]. Hence, in this study, E_{pitt} has been determined as the potential at which the current increases by an order of magnitude upon a 10 mV potential change [37]. Protection potential (E_{prot}) has been determined as the potential at which there is an abrupt change in

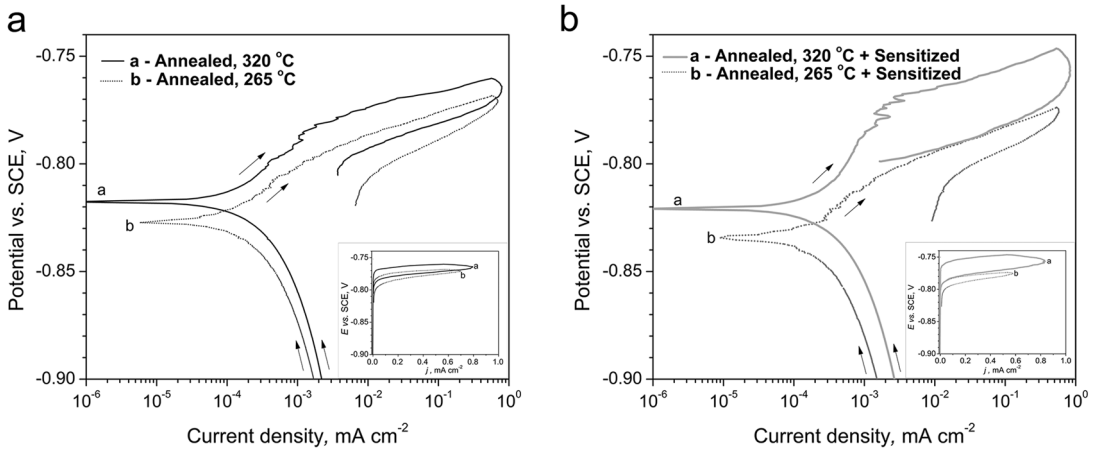

Figure 11. Potentiodynamic polarisation curves of annealed specimens before (a) and after (b) sensitisation. Insets show *E–j* dependence in linear coordinates

the inflection of the polarisation curve during the reverse sweep [34]. If the applied potential has a value above E_{prot} and is held constant, the current density would increase continuously, but if the applied potential is below E_{prot}, the current density will gradually decrease, i.e., pits will stop to grow [34]. The results show that the E_{ocp}, E_{pitt} and E_{prot} are slightly more negative for all specimens annealed at 265 °C than for ones annealed at 320 °C. However, $E_{pitt} - E_{prot}$ difference is significantly greater and, hence, charge density (q) for the sensitised specimens annealed at 320 °C than for the rest.

The Stern–Geary equation [38] has been applied to calculate corrosion current density. Polarisation resistance (R_p) (Table 4) has been determined in the LPR test. R_p corresponds to the slope of experimental curve E–j at the open circuit potential E_{ocp}. From the polarisation curve (Fig. 11), anodic (b_a) and cathodic (b_c) Tafel slopes have been determined. Cathodic Tafel slope is in a range 450–550 mV/dec for characterised states (Table 4). Due to the high value, cathodic Tafel slope has a small effect on corrosion current densities calculated by the Stern–Geary equation. The values of the anodic and cathodic Tafel slope (Table 4) are in good agreement with the literature data for aluminium alloys in neutral chloride solution [38–40]. Mechanism of the cathodic reaction is not clear. It is possible that the cathodic reaction has been controlled by oxygen diffusion towards the preferential sites for the oxygen reduction [35,41]. However, it is more likely that the cathodic reaction has been limited by electron transfer through the oxide film as in the case of aluminium [42]. Observed low values of the cathodic current density, 2–3 $\mu A/cm^2$ (Fig. 11) support the view that the reaction is controlled by the electron transfer. Thinning of the oxide film at more negative cathodic potentials enables easier electron transport and hence rate of cathodic reaction of oxygen reduction increases [42].

4 Discussion

The results of this study point out that the morphology of precipitated β-(Al_3Mg_2) phase plays more important role in the IGC and SCC susceptibility of the alloy than the amount of the precipitation. Despite six times smaller fraction of the precipitated Mg-rich phase, the difference clearly illustrated in Fig. 12, sensitised specimens annealed at 320 °C have poorer corrosion resistance due to the continuity of the grain boundary precipitation. According to Ref. [37], a presence of the continuous or closely spaced β-(Al_3Mg_2) phase at grain boundaries can trigger a pit spreading and formation of large clusters of corroded grain boundaries. The result is a greater charge flow due to the increased difference between potentials for a pit formation and inhibition of the pit growth. In this study, charge density (q) is two times greater for the almost continuous precipitation at the grain boundaries than when the precipitates are discrete (Table 4). However, other electrochemical parameters, such as corrosion potential, E_{ocp} (Table 4) do not reflect the observed trend. Slightly more negative values of the potentials of the specimens with a larger fraction of the precipitated anodic β-(Al_3Mg_2) phase, point out that IGC and SCC susceptibility are governed by local gradients and reactions in a vicinity of the grain boundaries and not average characteristics of the material as a whole.

Formation of the continuous precipitation along the grain boundaries appears to be related to the kinetic limitation imposed by the sensitisation temperature and lack of alternative diffusion paths in the fully recrystallised microstructure. Magnesium tendency to segregate at grain boundaries even at temperatures of full solubility [43] results in the grain boundaries sufficiently enriched in Mg to provide sites for a nucleation of fine crystallites (Fig. 7). However, precipitates' growth is confined to a narrow grain boundary region, i.e., in-plane growth (Fig. 7b and c), causing the formation of a nearly continuous film of uniform thickness (Figs. 5 and 6). The fine dispersion of crystallites, a majority of whom in the orientation of a single variant, or the film formed by their coalescence [44] gives grainy and non-uniform contrast in dark field TEM micrographs (Fig. 6), similar to the early stages of grain boundary precipitation in Al–Mg–Zn alloys [45]. The effect of dislocations, as alternative diffusion paths, is demonstrated by morphology and size of the precipitation in the specimens deformed of 2% prior sensitisation (Fig. 8). Similarly, in the study by Ref. [46], a thicker film has been observed in the vicinity of dislocations than in the dislocation free regions.

Sensitisation of the specimens annealed at 320 °C also affects grain boundary morphology by inducing transformation of initially curved grain boundaries into the faceted. In Al–Mg–Zn system, such faceting transition was observed in the presence of water vapour and was related to hydrogen segregation [47]. In the studied alloy, the in situ experiment shows that the faceting transition has been initiated as the precipitation took place at the grain boundary (Fig. 7). It is likely that the steps formation is a strain relaxation mechanism, since the grain boundary precipitation introduced significant strain fields into the surrounding

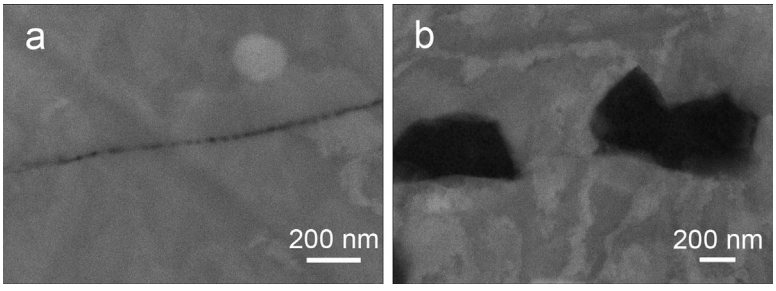

Figure 12. Backscattered electron SEM images of sensitised specimens showing distinct morphologies of precipitated β-(Al_3Mg_2) phase at grain boundaries: (a) annealed 3 h at 320 °C and (b) annealed 3 h at 265 °C

matrix (Fig. 6d) due to the large specific volume difference between β-(Al_3Mg_2) phase and Al matrix [44]. There are no other reports on the faceting transition in the Al–Mg system, but the observations of 'ribbon' or 'saw-tooth' morphology of the grain boundary precipitation [14,24] might be an indication of the faceting. The presence of the faceted grain boundaries could further facilitate crack propagation contributing to SCC susceptibility.

Precipitation of the anodic β-(Al_3Mg_2) phase during annealing at temperatures beyond Mg solvus [48], such as 265 °C, is the cause of a higher mass loss in the NAML test than in the precipitation free specimens annealed at 320 °C (Table 2). However, the precipitation is discrete (Fig. 9a) and the alloy is IGC resistant. Further growth and coarsening of the precipitate took place during the sensitisation. Recovered microstructure and greater dislocation density provides additional diffusion paths for Mg transport, so the growth is not limited to the in-plane direction of the grain boundaries. Particles also grew into the grain interior becoming coarse but still discrete (Figs., 10b and 12b). Apparently, continuous precipitate along the grain boundaries might not be a necessary condition for SCC susceptibility, but connectivity of the precipitates does play an important role in the material response to the corrosive environment. Also, the presence of anodic β-(Al_3Mg_2) phase within grain interiors contributes to a smaller potential gradient between grain boundaries and the matrix diminishing the driving force for the selective dissolution.

5 Conclusions

The effect of final annealing temperature and ensuing microstructure on the corrosion properties of the sensitised Al-6.8 wt% Mg alloy has been investigated.

1. The result of annealing at 320 °C is fully recrystallised microstructure without precipitates of β-(Al_3Mg_2) phase. During sensitisation, fine dispersoids forming a thin film-like coverage of grain boundaries precipitate. The sensitised material is SCC susceptible and has a very high mass loss in NAML test, i.e., becomes IGC susceptible.
2. Precipitation of the fine dispersoids at the grain boundaries induces a grain boundary faceting transition, most likely as a strain relaxation mechanism.
3. The annealing at 265 °C results in recovered microstructure and precipitation of β-(Al_3Mg_2) particles at the grain boundaries and interfaces of intermetallic particles. The β-(Al_3Mg_2) particles grew further during sensitisation, but remained discrete. The sensitised material is SCC resistant while the mass loss in NAML test is on the border line of IGC susceptible states.
4. The results show that the morphology of the grain boundary β-(Al_3Mg_2) phase has a greater effect on IGC and SCC susceptibility of the alloy than the fraction of precipitates.
5. Potentiodynamic measurements show that of all measured parameters charge density is in the best correlation with the NAMLT and SSRT results.

Acknowledgements: This research was supported by Ministry of Education, Science and Technological Development, Republic of Serbia, and Impol-Seval Aluminium Rolling Mill, Serbia, under contract grant TR 34018. Part of this work was performed at the National Center for Electron Microscopy, Lawrence Berkeley National Laboratory, and was supported by the Office of Science, Office of Basic Energy Sciences, of the U.S. Department of Energy under contract no. DE-AC02-05CH11231.

6 References

[1] J.R. Davis, (Ed.), *ASM Specialty Handbook: Aluminum and Aluminum Alloys*, ASM International, Materials Park, OH, USA **1993**.
[2] J. Hirsch, *Mater. Sci. Forum* **1997**, *242*, 33.
[3] S. A. Court, K. P. Hicklin, D. J. Lloyd, *Mater. Sci. Forum* **2002**, *396–402*, 1031.
[4] J. R. Davis, *Corrosion of Aluminum and Aluminum Alloys*, ASM International, Materials Park, OH, USA **1999**.
[5] L. I. Kaigorodova, *Mater. Sci. Forum* **1998**, *294–296*, 477.
[6] D. Tanguy, B. Bayle, R. Dif, Th. Magnin, *Corros. Sci.* **2002**, *44*, 1163.
[7] E. Pouillier, A.-F. Gourgues, D. Tanguy, E. P. Busso, *Int. J. Plasticity* **2012**, *34*, 139.
[8] R. K. Gupta, R. Zhang, C. H. J. Davies, N. Birbilis, *Corrosion* **2013**, *69*, 1081.
[9] R. H. Jones, J. S. Vetrano, C. F. Windisch, Jr, *Corrosion* **2004**, *69*, 1144.
[10] H. Yukawa, Y. Murata, M. Morinaga, Y. Takahashi, H. Yoshida, *Acta Metall. Mater.* **1995**, *43*, 681.
[11] R. H. Jones, D. R. Baer, M. J. Danielson, J. S. Vetrano, *Metall. Mater. Trans. A* **2001**, *32*, 1699.
[12] R. H. Jones, V. Y. Gertsman, J. S. Vetrano, C. F. Windisch, Jr, *Scripta Mater.* **2004**, *50*, 1355.
[13] J. L. Searles, P. I. Gouma, R. G. Buchheit, *Metall. Mater. Trans. A* **2001**, *32*, 2859.
[14] R. Goswami, G. Spanos, P. S. Pao, R. L. Holtz, *Metall. Mater. Trans. A* **2011**, *42*, 348.
[15] R. Goswami, R. L. Holtz, *Metall. Mater. Trans. A* **2013**, *44*, 1279.
[16] I. N. A. Oguocha, O. J. Adigun, S. Yannacopoulos, *J Mater. Sci.* **2008**, *43*, 4208.
[17] J. C. Chang, T. H. Chuang, *Metall. Mater. Trans. A* **1999**, *30*, 3191.
[18] J. C. Chang, T. H. Chuang, *J. Mater. Eng. Perform.* **2000**, *9*, 253.
[19] L. Tan, T. R. Allen, *Corros. Sci.* **2010**, *52*, 548–554.
[20] G. R. Argade, N. Kumar, R. S. Mishra, *Mater. Sci. Eng. A.* **2013**, *565*, 80.
[21] A. Halap, T. Radetić, M. Popović, E. Romhanji, *Metall. Mater. Trans. A* **2014**, *45*, 4572.
[22] T. Radetić, A. Halap, M. Popović, E. Romhanji, *Light Metal* **2014**, 297.
[23] X. H. Wang, J. H. Wang, J. Song, C. W. Fu, *Mater. Corros.* **2014**, *65*, 809.
[24] A. J. Davenport, Y. Yuan, R. Ambat, B. J. Connolly, M. Strangwood, A. Afseth, G. Scamans, *Mater. Sci. Forum* **2006**, *519–521*, 641.
[25] D. Scotto, D'Antuono, J. Gaies, W. Golumbfskie, M. L. Taheri, *Scripta Mater.* **2014**, *76*, 81.

[26] M. Popović, E. Romhanji, *J. Mater. Process. Tech.* **2002**, *125–126*, 275.
[27] M. Popović, E. Romhanji, *Mater. Sci. Eng. A* **2008**, *492*, 460.
[28] M. Popović, T. Radetić, E. Romhanji, in: H. Weil, A.D. Rollett, W.A. Cassada, (Eds.), *Proc.13th International Conference on Aluminum Alloys (ICAA13)*, TMS, Warrendale, PA **2012**.
[29] Y.-K. Yang, T. Allen, *Mater. Charact.* **2013**, *80*, 76.
[30] S. I. Vooijs, S. B. Davenport, I. Todd, S. van der Zwaag, *Philos. Mag. A* **2001**, *81*.
[31] W. Wei, S. Gonzales, T. Hashimoto, R. Prasath Babu, G. E. Thompson, X. Zhou, *Mater. Corros.* **2016**, *67*, 331.
[32] Y.-K. Yang, T. R. Allen, *Metall. Mater. Trans. A* **2013**, *44*, 5226.
[33] M. C. Carroll, P. I. Gouma, M. J. Mills, G. S. Daehn, B. R. Dunbar, *Scripta Mater.* **2000**, *42*, 335.
[34] K. Nisancioglu, H. Holtan, *Corros. Sci.* **1978**, *18*, 1011.
[35] E. Sikora, X. J. Wei, B. A. Shaw, *Corrosion* **2004**, *60*, 387.
[36] E. Kus, Z. Lee, S. Nutt, F. Mansfeld, *Corrosion* **2006**, *62*, 152.
[37] S. Jain, M. L. C. Lim, J. L. Hudson, J. R. Scully, *Corros. Sci.* **2012**, *59*, 136.
[38] F. Mansfeld, in: M.G. Fontana, R.W. Staehle, (Eds.), *Advances in Corrosion Science and Technology*, Vol.6, Plenum Press, New York, London **1976**.
[39] S. Papavinasam, in: L. Yang, (Ed.), *Techniques for Corrosion Monitoring*, Woodhead Publishing, Cambridge, England **2008**.
[40] R. Baboian, R. S. Treseder, (Eds.), *NACE Corrosion Engineer's Reference Book*, 3rd Edn., NACE International, Houston **2002**.
[41] J. R. Galvele, S. M. de DeMicheli, *Corros. Sci.* **1970**, *10*, 795.
[42] G. O. Ilevbare, J. R. Scully, *Corrosion* **2001**, *57*, 134.
[43] G. M. Scamans, N. J. H. Holroyd, C. D. S. Tuck, *Corros. Sci.* **1987**, *27*, 329.
[44] P. N. T. Unwin, R. B. Nicholson, *Acta Metall.* **1969**, *17*, 1379.
[45] J. K. Park, A. J. Ardell, *Acta Metall.* **1986**, *34*, 2399.
[46] Y. Zhu, D. A. Cullen, S. Kar, M. L. Free, L. F. Allard, *Metall. Mater. Trans. A* **2012**, *43*, 4933.
[47] W. Wunderlich, H.-J. Gudladt, *Acta Metall.Mater.* **1992**, *40*, 2123.
[48] V. Raghavan, *J. Phase Equilib. Diffus.* **2009**, *30*, 626.

(Received: October 16, 2015) W8709
(Accepted: December 17, 2015)

